

Ll.M. Evans, L. Margetts, V. Casalegno, L.M. Lever, J. Bushell, T. Lowe,
A. Wallwork, P. Young, A. Lindemann, M. Schmidt and P.M. Mummery

Transient thermal finite element analysis of CFC–Cu ITER monoblock using X-ray tomography data

Enquiries about copyright and reproduction should in the first instance be addressed to the Culham Publications Officer, Culham Centre for Fusion Energy (CCFE), K1/083, Culham Science Centre, Abingdon, Oxfordshire, OX14 3DB, UK. The United Kingdom Atomic Energy Authority is the copyright holder.

Transient thermal finite element analysis of CFC–Cu ITER monoblock using X-ray tomography data

L.I.M. Evans ^{a,b}, L. Margetts ^c, V. Casalegno ^d, L.M. Lever ^e, J. Bushell ^b, T. Lowe ^b,
A. Wallwork ^b, P. Young ^f, A. Lindemann ^g, M. Schmidt ^h and P.M. Mummery ^h

^a*CCFE, Culham Science Centre, Abingdon, Oxon, OX14 3DB, UK*

^b*School of Materials, University of Manchester, Grosvenor Street, Manchester M1 7HS, UK*

^c*School of Earth, Atmospheric and Environmental Sciences, University of Manchester, Williamson Building,
Manchester M13 9PL, UK*

^d*Department of Applied Science and Technology, Politecnico di Torino, Corso Duca degli Abruzzi 24,
I-10129 Torino, Italy*

^e*IT Services for Research, University of Manchester, Devonshire House, Oxford Road, Manchester M13 9PL,
UK*

^f*Simpleware Ltd., Bradninch Hall, Castle Street, Exeter, EX4 3PL, UK*

^g*NETZSCH-Gerätebau GmbH · Wittelsbacherstraße 42 · D-95100 Selb/Bayern, Germany*

^h*School of Mechanical, Aerospace and Civil Engineering (MACE), University of Manchester, Manchester
M13 9PL, UK*

Transient Thermal Finite Element Analysis of CFC-Cu ITER Monoblock Using X-ray Tomography Data

Ll.M. Evans^{a,b,*}, L. Margetts^c, V. Casalegno^d, L.M. Lever^e, J. Bushell^b,
T. Lowe^b, A. Wallwork^b, P. Young^f, A. Lindemann^g, M. Schmidt^h,
P.M. Mummery^h

^aCCFE, Culham Science Centre, Abingdon, Oxon, OX14 3DB, UK

^bSchool of Materials, University of Manchester, Grosvenor Street, Manchester M1 7HS, UK

^cSchool of Earth, Atmospheric and Environmental Sciences, University of Manchester, Williamson Building, Manchester M13 9PL, UK

^dDepartment of Applied Science and Technology, Politecnico di Torino, Corso Duca degli Abruzzi 24, I-10129 Torino, Italy

^eIT Services for Research, University of Manchester, Devonshire House, Oxford Road, Manchester M13 9PL, UK

^fSimpleware Ltd., Bradninch Hall, Castle Street, Exeter, EX4 3PL, UK

^gNETZSCH-Gerätebau GmbH · Wittelsbacherstraße 42 · D-95100 Selb/Bayern, Germany

^hSchool of Mechanical, Aerospace and Civil Engineering (MACE), University of Manchester, Manchester M13 9PL, UK

Abstract

The thermal performance of a carbon fibre composite-copper monoblock, a sub-component of a fusion reactor divertor, was investigated by finite element analysis. High-accuracy simulations were created using an emerging technique, image-based finite element modelling, which converts X-ray tomography data into micro-structurally faithful models, capturing details such as manufacturing defects. For validation, a case study was performed where the thermal analysis by laser flash of a carbon fibre composite-copper disc was simulated such that computational and experimental results could be compared directly. Results showed that a high resolution image-based simulation (102 million elements of 32 μm width) provided increased accuracy over a low resolution image-based simulation (0.6 million elements of 194 μm width) and idealised computer aided design simulations. Using this technique to analyse a monoblock mock-up, it was possible to detect and quantify the effects of debonding regions at the carbon fibre composite-copper interface likely to impact both component performance and expected lifetime. These features would not have been accounted for in idealised computer aided design simulations.

Keywords: X-ray tomography, finite element analysis, image-based modelling, thermal conductivity, laser flash, joining

1. Introduction

ITER, currently under construction, will be the world's largest nuclear fusion reactor. Its aim is to demonstrate the ability to produce an output power ten times that required to initiate fusion. Once operational, the plasma in which the reactions happen will subject the plasma facing components (PFCs) to around $10 \text{ MW}\cdot\text{m}^{-2}$ of thermal flux during steady-state operation. This value could be surpassed if plasma disruptions which release large amounts of energy over short time periods are not

* Corresponding author. Tel.: +44 1235 466524;
E-mail address: llion.evans@ccfe.ac.uk (Ll.M. Evans).

mitigated [1]. Therefore selection of materials for the PFCs is largely governed by their ability to withstand such a hostile environment whilst absorbing neutronic heating, minimising plasma impurities and protecting components shielded by the PFCs.

It is proposed that the divertor will consist of a series of flat armour tiles aligned in rows (see Fig. 1) with one side being plasma facing [3]. In order to remain within operational temperature limits the components must be actively cooled. This is achieved by connecting the tiles through their centres to a copper pipe carrying coolant (coined a monoblock). As the function of this heat sink is to transfer thermal energy away from the armour, it is imperative that the method of joining the armour to the pipe must provide a bond that retains both structural integrity and a high thermal conductivity under large thermal loads. As this region will contribute to, and potentially dominate, performance of the component, it is of utmost importance that the thermal behaviour at the armour-pipe interface is well characterised.

Until recently it was envisaged that the ITER divertor would include of two tiers; the armour for lower and upper parts consisting of carbon fibre composites (CFC) and tungsten (W) respectively [2]. Currently the ITER specifications are now for an all W divertor. This work concentrates on developing a non-destructive technique to predict ‘as-manufactured’ component performance. Although the case study in this report investigated CFC armour, the technique is material independent and could therefore be implemented on a wide range of machine critical components.

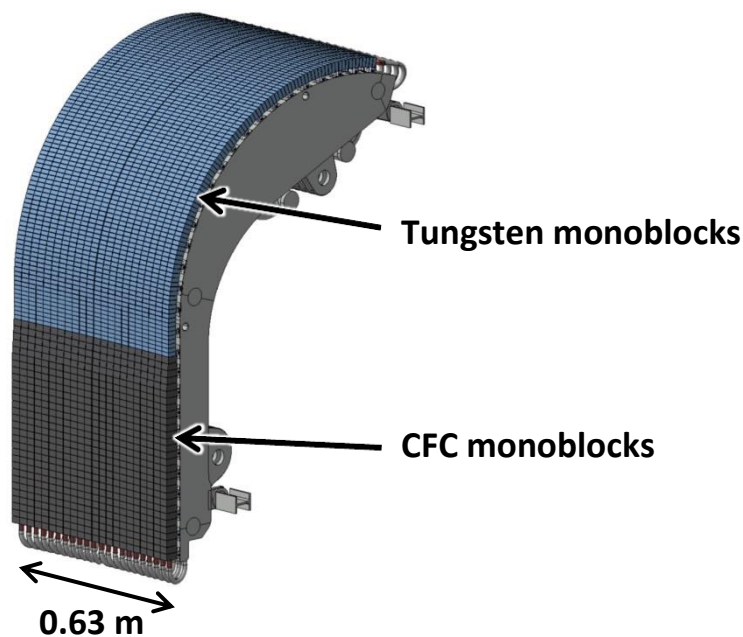


Fig. 1. Schematic of section from the early ‘two-tier’ ITER divertor [4].

Previous work has been carried out in order to characterise the thermal behaviour of a series of joining techniques for CFC-Cu samples [5]. The thermal performance across the interface has been investigated by measuring thermal diffusivity experimentally through laser flash analysis (LFA). Imaging by X-ray tomography provided high resolution images of the materials’ microstructures at the interface, providing insight as to how they might affect thermal behaviour. The most promising joining technique was the one developed at Politecnico di Torino [6]. The technique involves a low cost process that requires no applied pressure and can be performed at relatively low temperatures (i.e.

lower than required for Cu casting [7] or CFC modification [8]). The method uses a commercial braze (Gemco) which is modified by applying a layer of chromium. In joining, the braze is applied with the chromium face in contact with the CFC. When the component is heated the chromium reacts with the carbon to form chromium carbides. This leads to a better join between the CFC and the braze due to the improved wetting angle on chromium carbides, which would otherwise be poor.

In this paper, we explore the capabilities of a divertor monoblock mock-up manufactured using the Politecnico di Torino technique under reactor-like thermal loads. As this is difficult to carry out in the laboratory, we use Finite Element Analysis (FEA) to make our predictions.

FEA is usually performed by first creating a digital representation of the component using a computer aided design (CAD) package. This is typically a geometrically-ideal version of the component that does not include manufacturing flaws such as micro-cracking or porosity. In this paper we show that these imperfections play an important role in heat transfer. Creating the detailed models required is intractable using the CAD approach, so we use an emerging technique called Image-based Finite Element Modelling (IBFEM). IBFEM converts a three-dimensional image of a 'real' manufactured sample, including defects, into a digital geometry to be meshed for FEA. It has been shown that the IBFEM approach can give more accurate predictions than unit cell or analytical models [9]. Another benefit of the IBFEM technique is that direct comparison to experimental results can be made, as we can digitise for simulation the sample that has been subjected to laboratory tests [10].

This paper presents two case studies. The objective of the first case study is to verify and validate the technique. It involves comparing experimental and simulated results carried out on a simple "disc" shaped sample of CFC bonded to Cu subjected to Laser Flash Analysis (LFA). There are three simulations: (i) a CAD based model, (ii) a low resolution model generated from an X-ray Tomography scan and (iii) a high-resolution model generated from the same image. The CAD and low-resolution simulations can be carried out on a typical high end workstation, whilst the high resolution simulation requires access to supercomputing facilities. This exercise showed that the high resolution model provided the closest match to the experimental results. Therefore, the second case study uses high resolution IBFEM only to predict the behaviour of a CFC-Cu divertor monoblock mock-up under reactor-like thermal loads.

2. Materials

The CFC used was Sepcarb NB31 (Snecma Propulsion Solid, France). This is manufactured using a 3D NOVOLTEX preform needled in the z-direction with ex-pitch fibres and in x and y directions with ex-PAN fibres. Chemical vapour infiltration (CVI) is used for densification. The copper used was oxygen free high conductivity (OFHC) copper (Wesgo Metals, USA). The materials were joined by a brazing process using a Gemco® foil, 87.75 wt% Cu, 12 wt% Ge and 0.25 wt% Ni, (Wesgo Metals, USA). The foil was pre-coated with a 3 µm layer of chromium using radio frequency magnetron sputtering. The divertor monoblock was produced by drilling a hole in a CFC tile, inserting the Gemco foil and finally the copper pipe before brazing. Joining was performed at Politecnico di Torino as detailed by Casalegno et al [6].

In order to carry out the CFC-Cu disc case steady (the LFA experiment), further sample preparation was required. This was undertaken at The University of Manchester. The joined and individual samples, originally tile shaped, were machined using a lathe to produce cylindrical samples. A Struers Accutom-5 cut-off machine was used to obtain the thickness required for thermal analysis. The wheel was made of aluminium oxide and was set to rotate at 3000 rpm with a medium force and movement

of $2 \times 10^{-5} \text{ m}\cdot\text{s}^{-1}$. To clean the samples they were placed in an ultrasonic bath of acetone for 10 minutes.

Fig. 2 shows the samples in their prepared state. Table 1 details the resultant dimensions and properties. The samples' thickness and diameter were used to calculate the cylindrical volume, combined with mass this was in turn used to obtain density. Because these values included the porosity present within the CFC, reported values are for the bulk properties. Values for the constituent materials in the CFC-Cu disc were calculated from their respective thickness fractions. In this instance, the density values for CFC and Cu layers were obtained from an average of four CFC samples and the pure Cu sample respectively.

Scanning electron microscope (SEM) investigation of the CFC and brazing alloy interface (seen in Fig. 3) shows the formation of chromium carbide between the two layers. There is also infiltration of the carbide into open porosity on the surface.

Table 1
Sample dimensions.

Sample	Diameter (mm)	Thickness (mm)	Mass ($\times 10^{-3}$ kg)	Volume ($\times 10^{-6}$ m ³)	Density ($\times 10^3$ kg·m ⁻³)
CFC	12.66	2.06	0.447	0.2593	1.72
Cu	10.10	2.06	1.421	0.1650	8.61
CFC-Cu	12.70	4.84	2.916	0.6131	4.76
CFC(CFC-Cu)	12.70	2.74	0.631	0.3477	1.81
Cu (CFC-Cu)	12.70	2.10	2.285	0.2654	8.61

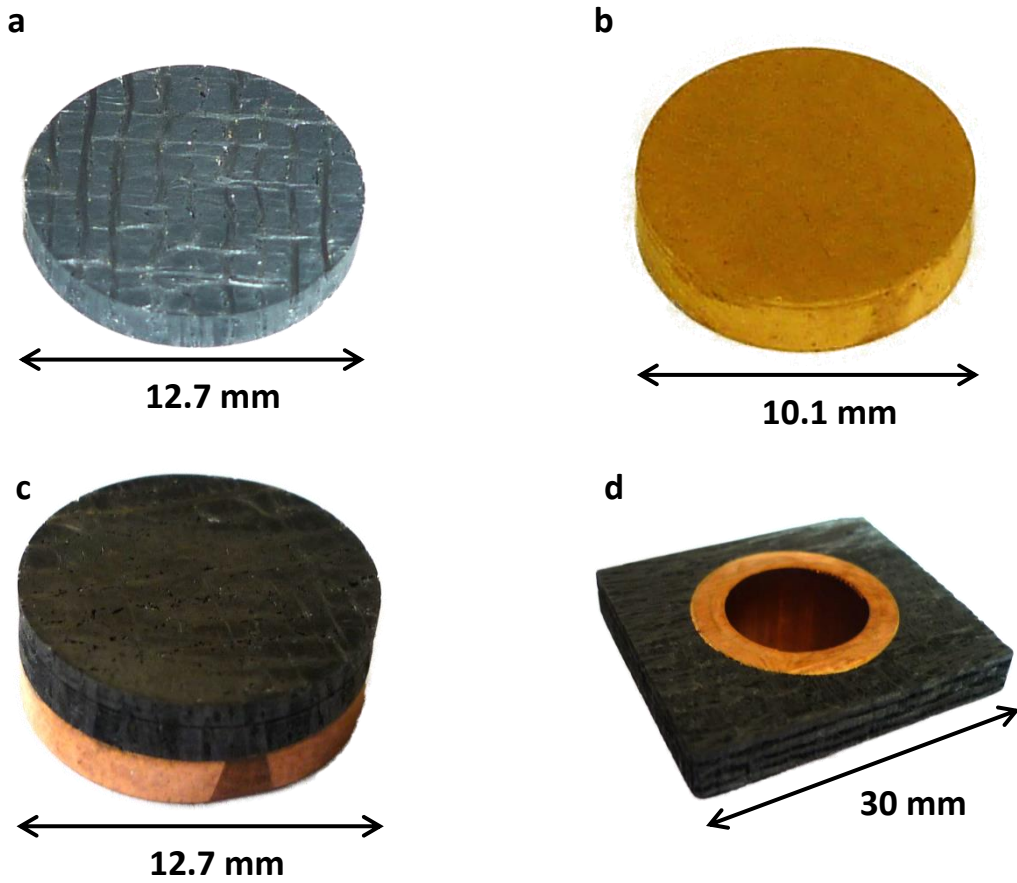


Fig. 2. Samples used; (a) CFC, (b) Cu, (c) CFC-Cu disc and (d) CFC-Cu divertor monoblock.

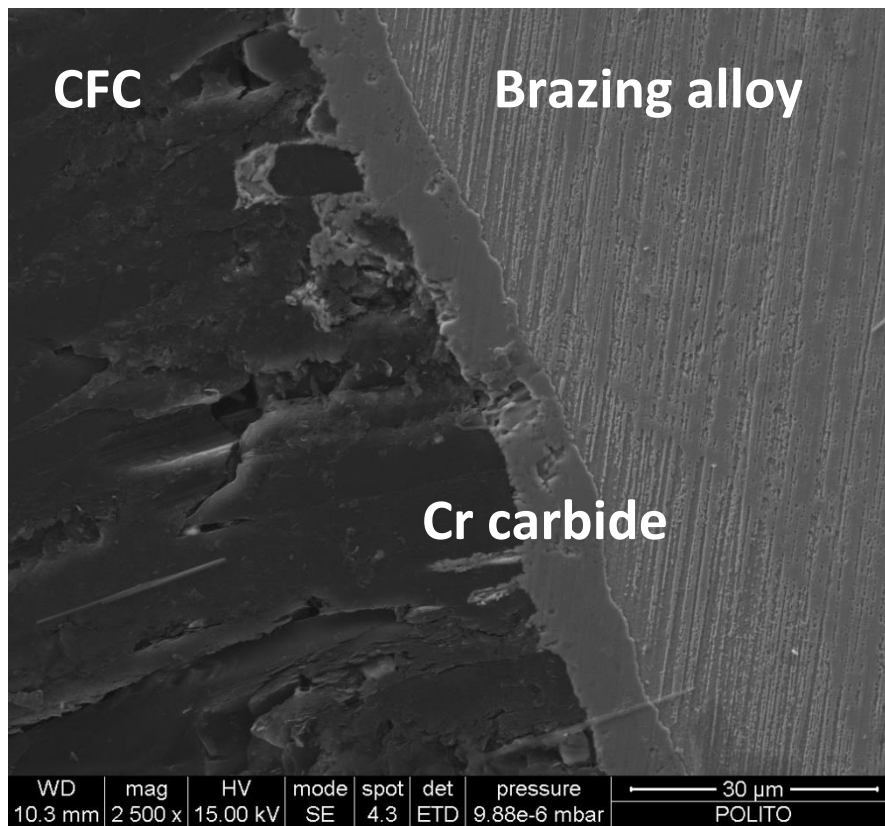


Fig. 3. SEM image of CFC and brazing alloy interface.

3. Method

This section details the (i) experimental determination of thermal properties using LFA, (ii) three-dimensional imaging using X-ray computed tomography, (iii) finite element mesh generation, (iv) definition of simulation boundary conditions, (v) equation solution and finally (vi) results analysis.

3.1 – Thermal diffusivity

The Netzsch 457 MicroFlash® system [11] was used to perform LFA. This system is used to irradiate the surface of a disc shaped sample of known thickness with a short laser pulse. The time the heat pulse takes to travel through the sample is measured by an infra-red camera directed at the rear face. This is used to calculate thermal diffusivity. Specific heat and thermal conductivity can be calculated by comparing results with a calibration sample.

To ensure stability of the sample and maximum absorption of energy from the pulse, measurements were performed in an inert atmosphere after the sample had been coated with graphite. Results were collected at intervals of 100 °C, ranging from 100 °C to 700 °C. The average of 5 measurements at each interval was recorded.

3.2 – X-ray tomography

The Nikon Metrology 225/320 kV system (using the 225 kV source) at the Manchester X-ray Imaging Facility [12], University of Manchester, UK, was used to create X-ray tomography scans of the CFC-Cu disc and the divertor monoblock. Imaging and reconstruction settings are shown in Table 2 and Table 3 respectively. Voxel widths of 9.7 µm and 21.8 µm were achieved for the CFC-Cu disc and divertor monoblock respectively. However, due to signal noise, not all features at these scales were resolvable e.g. the 10 µm layer of chromium on the braze.

Table 2

X-ray tomography parameters used.

Sample	Target	Voltage (kV)	Current (µA)	Filter (mm)	Acquisition Time (s)	Number of Projections	Frames / Projection
CFC	Cu	120	200	N/A	0.5	2001	1
Cu	W	220	210	Sn, 1.0	0.7	3142	1
CFC-Cu	W	210	135	Sn, 1.0	1.415	2001	2
Monoblock	W	200	190	Ag, 1.0	1.415	2001	2

Table 3

Reconstruction settings.

Sample	Beam Hardening	Noise Reduction	Voxel Width (x 10 ⁻⁶ m)
CFC	1	3	10.0
Cu	2	2	8.2
CFC-Cu	2	4	9.7
Monoblock	1	2	21.8

3.3 – Finite element mesh generation

The CFC-Cu disc and divertor monoblock scans were imported into the Simpleware [13] suite of programmes, version 6 (Simpleware Ltd., Exeter, Devon, UK) to convert the 3D images into FE meshes. Image segmentation was performed using a range of techniques including the flood-fill, cavity fill, island removal, manual paint tools and a recursive Gaussian smoothing filter. Linear 4-node tetrahedral elements were selected for meshing.

A low resolution and high resolution mesh was created for the CFC-Cu disc case study. The low resolution mesh captured the main features, such as surface roughness and large pores. The resolution of the higher fidelity model was carefully chosen, striking a balance between capturing fine details of the micro-structure and producing a model that could be easily handed on the various computer platforms available. Creating a finite element model at the same resolution as the original tomography scan is technically challenging and probably offers little benefit over the high resolution model selected.

A CAD version of the CFC-Cu disc was created and meshed in Abaqus, version 6.12 (Simula, Providence, RI, USA). This model comprised a cylinder with three layers of varying thickness representing the CFC, Gemco and Cu. Porosity was not included. The CAD based mesh had approximately 50,000 tetrahedral elements (consistent with typical engineering practice).

As the results presented later show, the high resolution model gives the closest match to the LFA experiment carried out on the CFC-Cu disc. Therefore, only a high resolution model was created for the divertor monoblock case study.

3.4 – Finite Element Analysis

3.4.1 – Boundary conditions for CFC-Cu disc

In order to recreate the LFA experiment *insilico*, a thermal load matching the laser's must be applied to one surface of the finite element model whilst the temperature values on the opposite side are recorded with respect to time. In order to determine the magnitude and distribution of the load we must consider the laser's operation.

Experimental measurements showed that, at the operating voltage 1538 V, the laser delivered 6 J over the duration of the laser pulse (see Fig. 4). The measurements were made without the optics in place. The LFA 457 has 3 focusing lenses, which cause an attenuation of approximately 5 % per surface (i.e. 6 lens surfaces). Thus, the resultant energy incident from a single pulse on the sample over a 15 mm diameter spot size is 5.8 J.

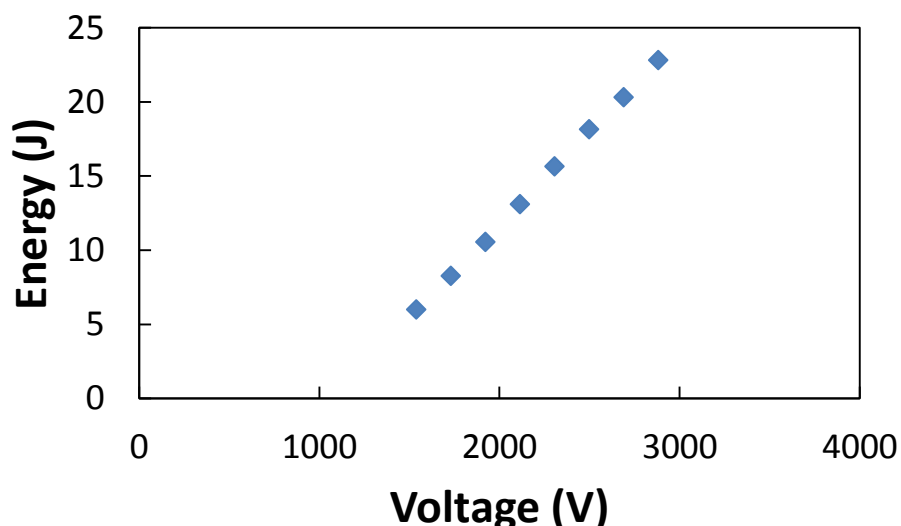


Fig. 4. Laser energy for a given voltage for the NETZSCH LFA 457.

Fig. 5 shows the energy amplitude of a typical laser shot for a given applied voltage. As no calibration data was available to link applied voltage to laser energy output, the energy amplitude is therefore normalised between minimum and maximum values. The total energy output of the laser (calculated

above to be 5.8 J) is the area under the curve in Fig. 5. Thermal flux, the rate of energy transfer per unit of area, has the units $\text{J}\cdot\text{m}^{-2}\cdot\text{s}^{-1}$. By knowing the total energy emitted over a certain area, it is possible to calculate the flux;

$$\text{i.e. peak flux} = \text{total energy (J)} / (\text{spot area (m}^2) * \text{area under curve (s)})$$

This can be used with the non-dimensionalised amplitude curve to produce a flux profile with respect to time i.e. the curve in Fig. 5 using the secondary axis values.

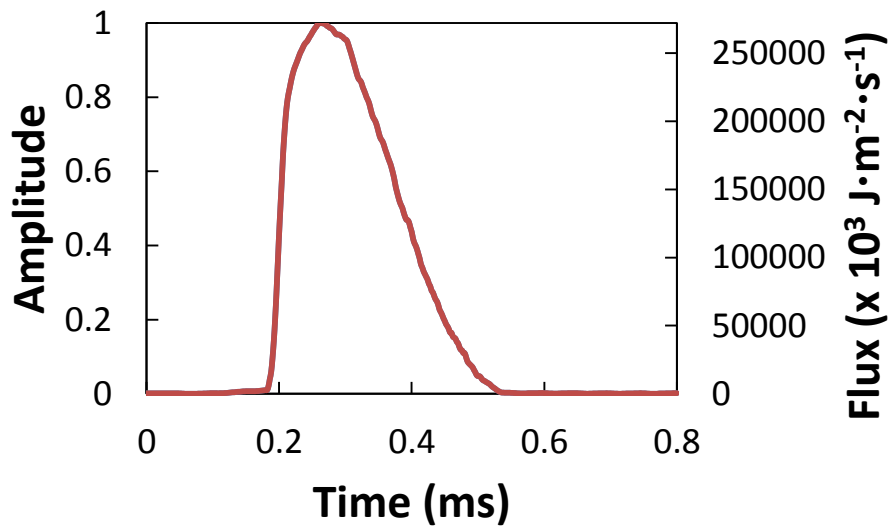


Fig. 5. Typical energy pulse emitted from NETZSCH LFA 457 laser.

Flux is a quantity which applies to an area, but due to the discretisation in finite element analysis it must be applied at nodal points. Thus the equivalent flux value for an area must be projected to the nodes defining that area. Assuming the discretised area is sufficiently small the flux value over that area can be considered uniform. For first order finite elements, the projected flux value at the node is calculated by dividing the total flux equally between each of the nodes, as shown in Fig. 6 [14]

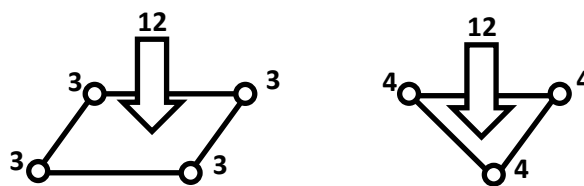


Fig. 6. Projecting flux over an area to nodal coordinates due to discretisation inherent in FEA.

An additional consideration for the LFA scenario is that the surface onto which the laser is incident is not completely flat. Element faces describing this surface will be oriented at different angles in three-dimensional space. The laser path is considered to travel purely in the z-direction and will not arrive normal to the element face. Therefore it is important to calculate the effective elemental area in the x-y plane, as this is the area 'seen' by the laser. A simple example of a surface consisting of 4 triangular elements is shown in Fig. 7. Even in such a simple case, the three dimensional area is 30% greater than the effective 2D area in the x-y plane.

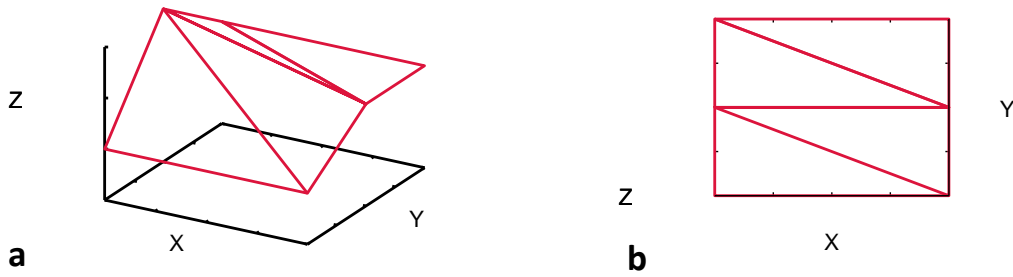


Fig. 7. Comparison of the area of (a) element faces and (b) the effective area seen by the laser in x-y plane.

The 3D area is calculated by taking the cross product of any two of the three vectors defining the triangle, where A, B & C are the nodes.

$$area = \left| \frac{\overrightarrow{AB} \times \overrightarrow{AC}}{2} \right|$$

(1)

In 2D this simplifies to

$$A_{el} = \left| \frac{A_x(B_y - C_y) + B_x(C_y - A_y) + C_x(A_y - B_y)}{2} \right|$$

(2)

Therefore, the nodal contribution from a tetrahedral element as a fraction of the whole domain would be $\frac{1}{3} \frac{A_{el}}{A_{tot}}$ where A_{el} is the area of the element face and A_{tot} is the area of the surface being thermally loaded.

These values assume a uniform distribution of flux over the whole sample surface area. Lasers typically exhibit a Gaussian distribution of their beams, as shown in Fig. 8.

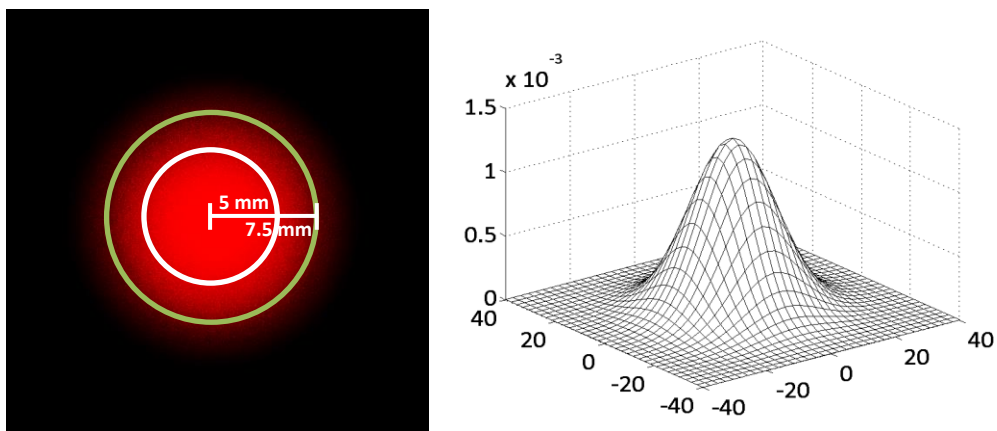


Fig. 8. Multivariate Gaussian distribution exhibited by laser beam.

In 2D this is known as the multivariate Gaussian distribution (MGD) (3).

$$f(x, y) = \frac{1}{2\pi\sigma_x\sigma_y\sqrt{1-\rho^2}} \exp\left(-\frac{1}{2(1-\rho^2)}\left[\frac{(x-\mu_x)^2}{\sigma_x^2} + \frac{(y-\mu_y)^2}{\sigma_y^2} - \frac{2\rho(x-\mu_x)(y-\mu_y)}{\sigma_x\sigma_y}\right]\right) \quad (3)$$

where σ_x, σ_y are the standard deviation in x and y directions, ρ is the correlation between x & y and μ_x & μ_y are the mean values. For the case of the laser beam $\sigma_x = \sigma_y$ and ρ, μ_x & μ_y are zero. Therefore (3) simplifies to (4) and in polar coordinates (5).

$$f(x, y) = \frac{1}{2\pi\sigma^2} \exp\left(-\frac{x^2 + y^2}{2\sigma^2}\right) \quad (4)$$

$$f(r) = \frac{1}{2\pi\sigma^2} \exp\left(-\frac{r^2}{2\sigma^2}\right) \quad (5)$$

As the CFC-Cu disc is smaller than the laser spot size, calculating the total energy delivered must take into consideration the non-uniform distribution. Additionally the applied nodal loads must reflect this spatial variation in distribution.

According to the LFA 457 manufacturers, it can be expected that the laser power reduces by 10 % of the peak value 5 mm from the centre. This is observed when the standard deviation is 10.892 (see Fig. 9). In order to use the profile in Fig. 9 to calculate the thermal loads to be applied, the peak energy needs to be determined, i.e. where $r = 0$ mm. To do this it must be ensured that the volume under the 2D MGD (between -7.5 and 7.5 in x and y) is equal to the volume under the uniform distribution over the same area. That is, within a given time-step, the amount of energy delivered is equal to the uniform distribution calculation. This volume can also be seen as ‘power’ which has the units $J \cdot s^{-1}$.

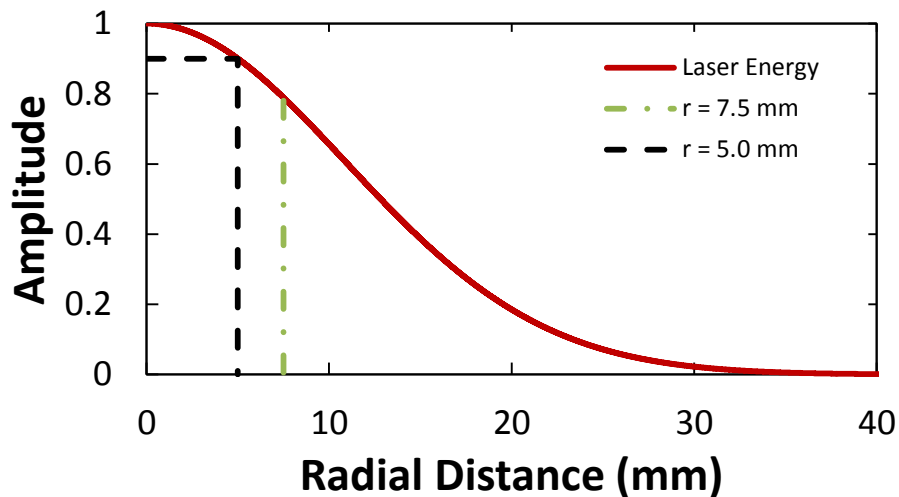


Fig. 9. MGD profile of 15 mm diameter spot size laser where energy reduces by 10 % between centre and $r = 5.0$ mm, i.e. $\sigma = 10.892$.

To calculate the volume under the MGD we must integrate the equation describing the curve over the whole region, R , using polar coordinates as shown in equation (6).

$$V = \iint_R f(x, y) dA = \iint_R f(r) r dr d\theta$$

$$\iint_R f(r) r dr d\theta = 1 - \exp - \frac{1}{2} \left(\frac{r}{\sigma} \right)^2$$

(6)

When calculated to infinity, the volume under the MGD is unity. However, for this purpose it is necessary for the distribution delivered over the 15 mm diameter spot size to be unity. Therefore, a normalising factor, F_n , is required. This is given as the ratio of the volumes of the two distributions where 'r' is infinity and 7.5.

i.e.

$$V_{\infty} = 1, V_{7.5} = 0.211$$

$$F_n = \frac{V_{\infty}}{V_{7.5}} = 4.738$$

$$V_{7.5} F_n = 1$$

Thus, the flux at any point can be described as a function of its distance from the origin

$$\Phi(r, t) = F_n f(r) P_t$$

where P_t is the power for a given time step, calculated by multiplying the flux for a given time step, Φ_t , (as found above, see Fig. 5) by the spot size area ($P_t = \Phi_t * \pi R^2$).

Combining the above for a triangular face on a tetrahedral element, the flux for a particular node at any given time step is;

$$\Phi(r, t) = \frac{1}{3} \frac{A_{el}}{A_{tot}} \frac{F_n}{2\pi\sigma^2} \exp \left(- \frac{r^2}{2\sigma^2} \right) P_t$$

(7)

The MGD is a function of the distance of the node from the central point of the sample. The radial distance, r , is defined as (8) where the nd and c subscripts denote the nodal and central x-y coordinates.

$$r = \sqrt{(x_{nd} - x_c)^2 + (y_{nd} - y_c)^2}$$

(8)

As this calculation must be repeated over all elements on the surface where the laser is incident, it is probable that a single node will receive a contribution from several adjacent elements. In this case, the values are summed to give a total nodal flux.

3.4.2 Case Study 1: CFC-Cu disc

Once the method for specifying the boundary conditions had been determined, verification and validation of the IBFEM technique could be performed by comparing experimental and simulated

results of the LFA for the CFC-Cu disc sample. The CAD-based model, together with the low resolution IBFEM and high resolution IBFEM models were analysed using ParaFEM (revision 1796), an open source parallel finite element platform developed by the authors [14] [15] [16] [17] [18].

To ensure an accurate non-oscillatory (stable) solution a time step of 2×10^{-6} s was used together with an iterative solver stopping criterion of 1×10^{-6} .

The Laser Flash experiment was simulated at a furnace temperature of $200 \text{ }^\circ\text{C}$, using the material properties measured by LFA for CFC and Cu. Properties for Gemco were obtained from the manufacturer [19] and standard values for air [20] were used for the porosity.

3.4.3 Case Study 2: Divertor monoblock

In the second case study, the performance of the divertor monoblock was investigated under reactor-like thermal loads. Several design scenarios exist for ITER each with their own set of in-service parameters. Here, the transient response of the divertor monoblock going from initial state to steady-state operation was modelled.

A thermal flux of $10 \text{ MW}\cdot\text{m}^{-2}$ was applied to one outer CFC surface of the divertor monoblock to simulate the thermal load from the plasma. To represent a coolant running at $150 \text{ }^\circ\text{C}$ the inner surface of the Cu pipe was fixed to the same temperature (see Fig. 10). The CFC surface was selected such that fibre orientation matched that of the CFC-Cu disc modelled in the first case study. Initial temperature was set to $150 \text{ }^\circ\text{C}$ throughout the domain, to match that of the coolant. The simulation was run using gradually increasing time-step sizes until steady-state operation was achieved. This was to ensure that the temperature changes at the start of the simulation, where changes are at their greatest, were accurately captured whilst computational expense was reduced as the simulation neared equilibrium. Details for time step size can be found in Table 4 and an iterative solver stopping criterion of 1×10^{-6} was used. The results of both case studies were post-processed using ParaView, version 3.14.1 64-bit (Kitware Inc., Clifton Park, New York, USA) [21].

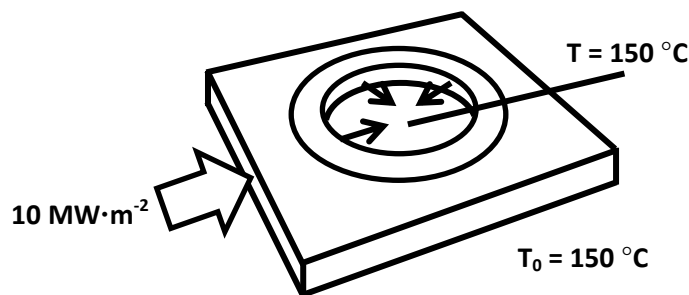


Fig. 10. Schematic of applied loads and temperatures in monoblock simulation.

Table 4

Details of time step sizes used.

Time step size (s)	Number of steps	Total sum of time (s)
0.000001	100	0.0001
0.000005	80	0.0005
0.00001	50	0.001
0.00005	80	0.005
0.0001	50	0.01
0.0005	80	0.05
0.001	50	0.1
0.005	80	0.5
0.01	50	1
0.05	40	3
0.1	20	5

4. Results and discussion

This section presents (i) the thermal diffusivity values determined experimentally for the constituent materials and the CFC-Cu disc; (ii) micro-structural observations regarding the CFC-Cu interface in both the CFC-Cu disc and the divertor monoblock; (iii) quantitative and qualitative analysis of the image-based meshing technique and (iv) results of the finite element analyses for the CFC-Cu disc and the divertor monoblock.

4.1 Thermal Diffusivity

Fig. 11 shows the thermal diffusivity results measured experimentally by LFA. Fig. 12 and Fig. 13 chart the specific heat and thermal conductivity values calculated by calibration with the reference sample. The figures present results for the constituent materials, the projected values for the CFC-Cu disc based on the contributions by thickness of each material and finally the actual values measured for the CFC-Cu disc. The results for the constituent materials are comparable to those found in the ITER materials property handbook (IMPH) [22], shown in Table 5.

Comparing the projected and actual thermal conductivity for the CFC-Cu disc, it can be seen that the measured conductivity is considerably lower than expected. The CFC appears to restrict heat flow, with the conductivity of the combined sample being only slightly higher than that of CFC. This is despite 43% of the sample's thickness consisting of the more highly conducting Cu. Interestingly, over the temperature range of 600 °C the conductivities of the CFC and Cu decrease by 45% and 20%, respectively. Thus, the average change would be a decrease of 34%, which is very close to the actual decrease of 35%.

The IMPH specifies that the thermal conductivity must be greater than $300 \text{ W}\cdot\text{m}^{-1}\cdot\text{K}^{-1}$ at room temperature and only decreasing to $150 \text{ W}\cdot\text{m}^{-1}\cdot\text{K}^{-1}$ at 1000 °C. This is partly because it has been shown that plasma erosion decreases in CFCs with higher thermal conductivity [23], which ensures increased longevity for component life cycles. This component does not quite meet the specified criterion, $273 \text{ W}\cdot\text{m}^{-1}\cdot\text{K}^{-1}$ at 100 °C (projected to be $288 \text{ W}\cdot\text{m}^{-1}\cdot\text{K}^{-1}$ at room temperature) and $178 \text{ W}\cdot\text{m}^{-1}\cdot\text{K}^{-1}$ at 700 °C (projected to be $162 \text{ W}\cdot\text{m}^{-1}\cdot\text{K}^{-1}$ at 100 °C), but is relatively close.

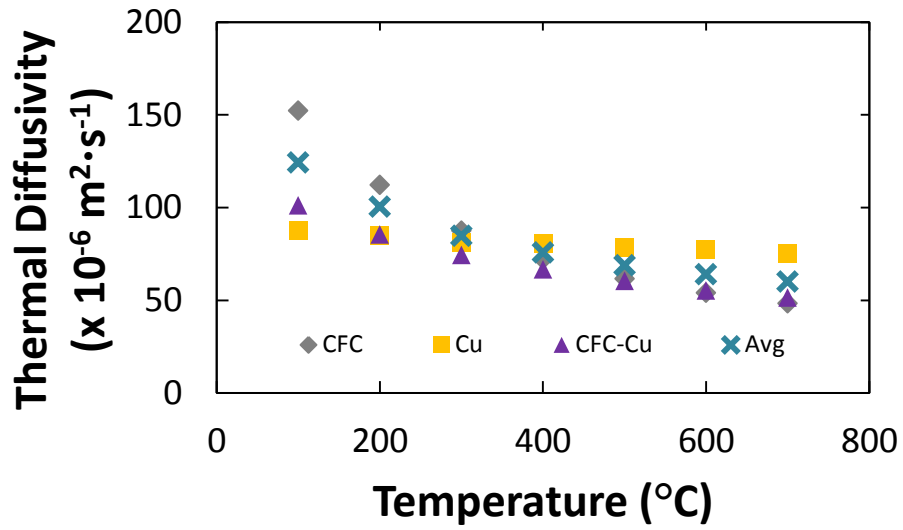


Fig. 11. Thermal diffusivity measured by laser flash analysis.

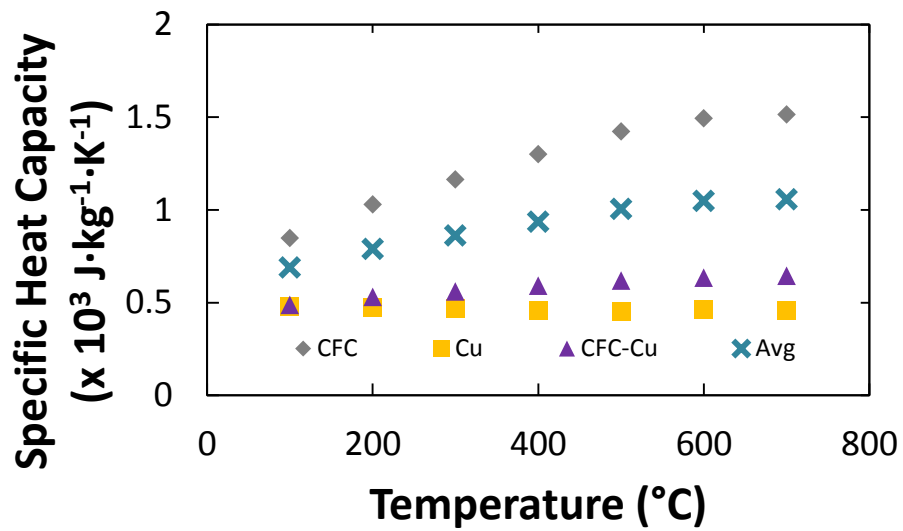


Fig. 12. Specific heat capacity calculated by calibration of diffusivity against Pyroceram 9606.

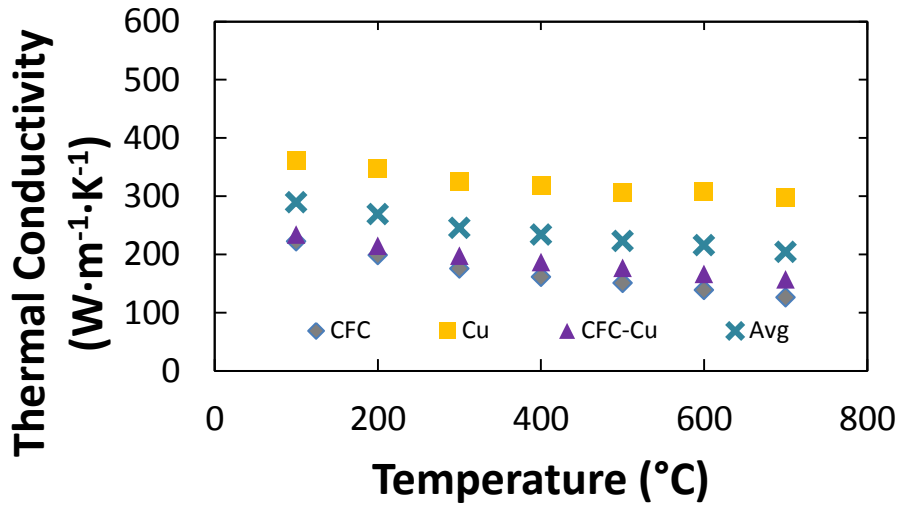


Fig. 13. Thermal conductivity calculated from diffusivity, density and specific heat values.

Table 5

Materials properties of CFC and Cu as specified by IMPH.

Properties	T (°C)	CFC (z direction)	Cu
Thermal conductivity (W·m ⁻¹ ·K ⁻¹)	RT ⁺	304	379
	250 / 200	240	355
	800 / 350	145	351
	1000 / 500	141	357
Specific Heat (x 10 ³ J·kg ⁻¹ ·K ⁻¹)	RT	0.780	0.388
	800 / 200	1.820	0.400
	1000 / 500	2.000	0.437
CTE (x 10 ⁻⁶ K ⁻¹)	800 / 200	0.4	17.0
	1000 / 500	0.5	18.6
Density (x 10 ³ kg·m ⁻³)	RT	1.90	8.90
Porosity (%)	RT	8	N/A

⁺ Room temperature

4.2 X-ray tomography images

Fig. 14 shows that the Cu at the interface of the CFC-Cu disc is rough. In certain regions small veins of Cu rise from the surface. This shows that the brazing material does not remain in its initial position but contorts to the shape of the CFC and even fills open porosity. This greatly increases the interface surface area from $126.7 \times 10^{-6} \text{ m}^2$ if smooth, calculated geometrically, to $132.2 \times 10^{-6} \text{ m}^2$, measured from the X-ray tomography image. It is expected that this enhances both bond strength and thermal transport across the interface. The majority of the Cu at the surface (80.4 %) is in contact with the CFC, therefore it can be assumed that the bonding will be successful in maximising thermal conductivity.

In contrast, the X-ray scan for the divertor monoblock shows debonding on one side of the pipe (see Fig. 15). It appears that this area is linked with the orientation of the sample during the brazing process i.e. the divertor monoblock was on its side during joining and the upper surface is where the pipe has pulled away most probably due to a combination of the effects of gravity and a mismatch in thermal expansion coefficient between the CFC and Cu. It is expected that this region will act as a substantial thermal barrier during operation.

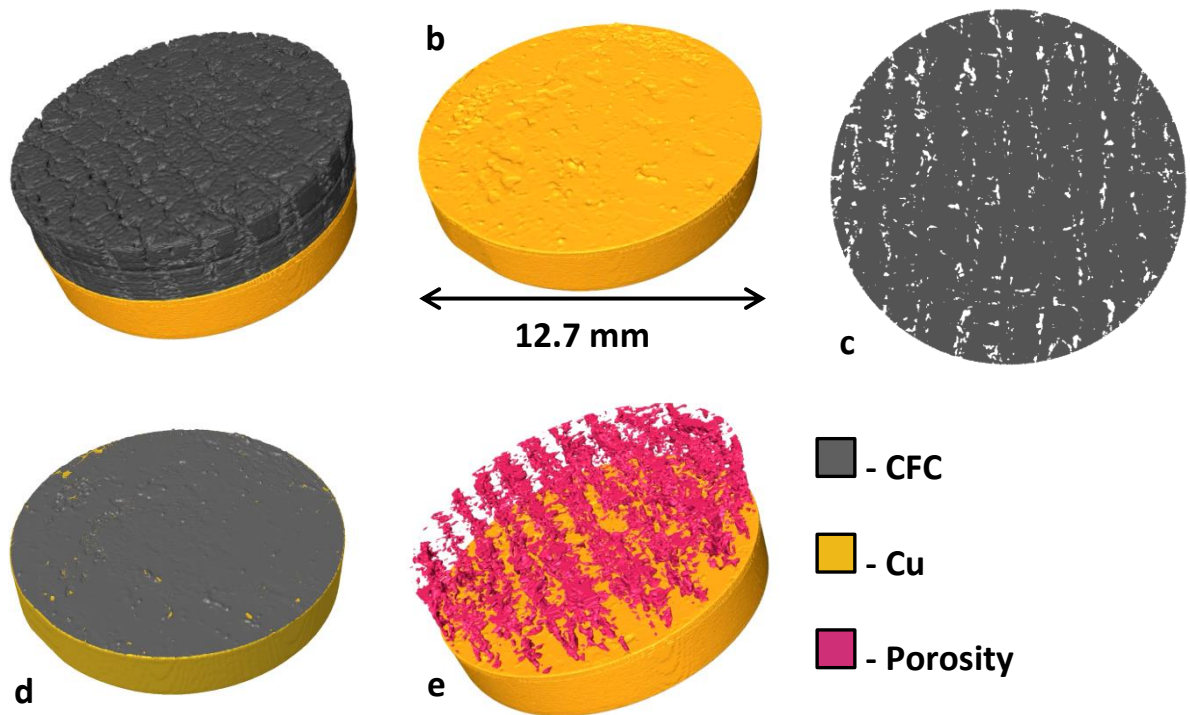


Fig. 14. 3D reconstruction from X-ray tomography data for the CFC-Cu disc showing; (a) complete sample, (b) rough Cu surface at interface with CFC, (c) slice midway through CFC section, (d) contact area at CFC-Cu surface and (e) porosity within the CFC showing preferential alignment with direction of thermal transport.

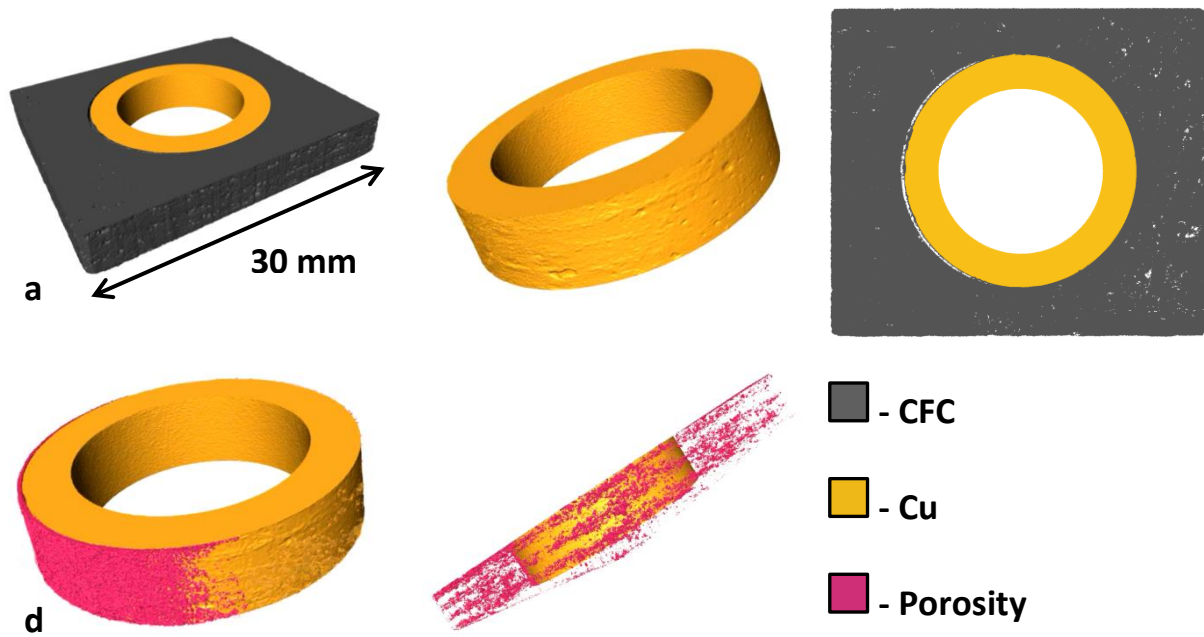


Fig. 15. 3D reconstruction from X-ray tomography data for divertor monoblock showing; (a) complete sample, (b) rough Cu surface at interface with CFC, (c) slice through the midplane, (d) large area where CFC has debonded from Cu during brazing process and (e) porosity within the CFC showing preferential alignment with direction of thermal transport.

Pores within CFCs are an unavoidable issue. They affect thermal conductivity by behaving as thermal barriers. The greatest concentration of porosity is typically found aligned between fibre layers. Thus, through design of the composite layup, it is possible to arrange these layers to give directionally preferential performance. It can be seen that the porosity in the divertor monoblock is aligned to promote thermal transport radially away from the pipe.

4.3 Conversion of tomography data into finite element meshes

The automatic segmentation tool used by Simpleware [13] can segment images into different phases according to the voxel greyscale values. It was possible to segment the majority of the images automatically. Because of noise at the CFC-Cu interface and ring artefacts in the CFC, additional attention was required. Segmentation was carried out manually using paint/un-paint tools on a slice by slice basis. Before meshing, the images were downsampled, reducing computational cost whilst retaining micro-structural detail (see Fig. 16).

Considering the CFC-Cu disc, at 30 % resolution, there is little difference in visible detail when compared with the full resolution achieved in the scan (100 %). A lower resolution (5%), suitable for analysis using a workstation, loses many features.

Details characterising the models are given in Table 6 and Table 7 for the CFC-Cu disc and divertor monoblock respectively.

As the image comprises voxels (cuboids), smoothing is applied in meshing to better describe the curved nature of the geometry. This can cause quantities derived from the mesh geometry to differ from those derived from the original image. Changes in volume and surface area for all meshes are recorded in Table 6 and Table 7 as a percentage of those values at the original resolution. The total volumetric changes can be considered negligible.

When considering volumetric changes within the constituent materials there are two notable changes. Firstly, in the low resolution mesh, the Gemco layer is greatly increased by over 400 % in the CFC-Cu disc. The reason for this is that when downsampled, the layer becomes smaller than one voxel width. To retain the feature, it had to be artificially dilated (using the software) to the thickness of the new voxel width, resulting in the increase in volume. It is expected that this will affect the simulated conductivity at the interface because the conductivity of Gemco is lower than both CFC and Cu (see Table 8). Secondly, there is a decrease in porosity at each downsampling level, 28 % then 90 % for the CFC-Cu disc and 81 % for the divertor monoblock. This is because some of the pores are smaller than the new voxel widths. This should cause the simulated sample to have an artificially increased conductivity due to the loss of thermal barriers in the form of porosity (confirmed later in Fig. 18).

The surface area of the models decreases with increasing levels of downsampling. This can be attributed to a reduction in surface detail as the image resolution decreases. The greatest variation can be seen in the CFC and porosity.

A few additional observations can be drawn from the segmented image statistical data. When comparing the total volume of the CFC-Cu disc with that calculated geometrically (see Table 1), the values agree to within 3 %. The porosity fraction of the CFC-Cu disc is 7.5 %, which closely agrees with the literature value of 8 %. However, this reduces to 1.2 % for the divertor monoblock because of the lower initial image resolution. Overall, the high resolution meshes were acceptable.

For the CFC-Cu disc, meshes with 0.6 million and 102 million elements were produced for the low and high resolution models, respectively. For the divertor monoblock, the high resolution mesh comprised 137 million elements. These numbers were within the target range for use on a laboratory workstation (low resolution) and modern supercomputer (high resolution).

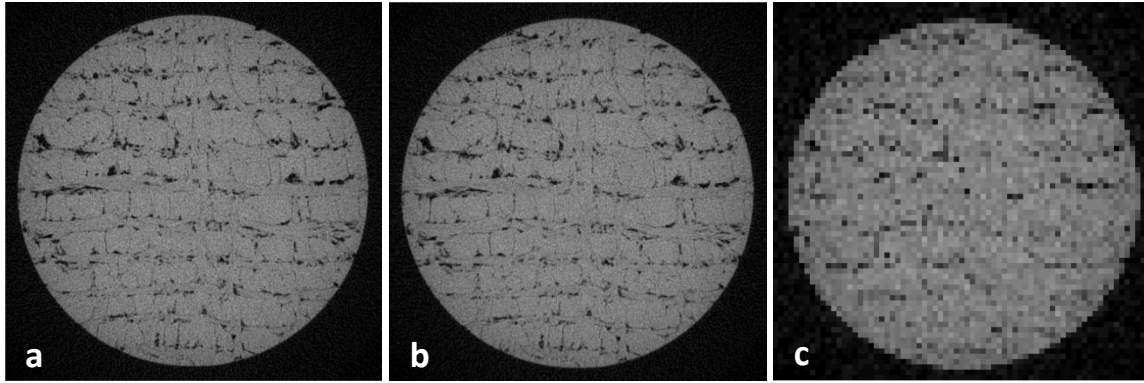


Fig. 16. X-ray tomography slice of CFC showing effect of downsampling from (a) original resolution to (b) 30% and (c) 5% resolutions.

Table 6

Segmentation and meshing output details for the CFC-Cu disc.

Name	Number of Voxels	Segmented Volume ($\times 10^{-9} \text{ m}^3$)	Surface area ($\times 10^{-6} \text{ m}^2$)	Number of Elements	Number of Nodes	Meshed Volume ($\times 10^{-9} \text{ m}^3$)
CFC-Cu (Original resolution, $9.7 \times 10^{-6} \text{ m}$ voxel width)						
Cu	289 M	264	478			
CFC	326 M	298	2600			
Porosity	26 M	24	1910			
Gemco	6.3 M	5.78	357			
Total	642 M	592	4988			
CFC-Cu (30% resolution, $32.3 \times 10^{-6} \text{ m}$ voxel width)						
Cu	7.8 M	-0.38%	-5.65%	40 M	8.2 M	-0.16%
CFC	8.8 M	-0.34%	-17.69%	53 M	11 M	1.40%
Porosity	0.70 M	-0.83%	-18.85%	7.1 M	2.2 M	-27.68%
Gemco	0.17 M	-1.38%	-10.64%	1.8 M	0.47 M	-5.23%
Total	17 M	-0.39%	-10.59%	102 M	22 M	-0.54%
CFC-Cu (5% resolution, $194.0 \times 10^{-6} \text{ m}$ voxel width)						
Cu	35 k	-3.79%	-12.97%	206 k	46 k	-4.85%
CFC	38 k	-6.38%	-63.00%	307 k	63 k	-2.79%
Porosity	3 k	-1.25%	-69.79%	29 k	17 k	-90.45%
Gemco	4 k	496.89%	-13.17%	46 k	12 k	460.52%
Total	81 k	-0.10%	-54.59%	587 k	137 k	-2.74%

Table 7

Segmentation and meshing output details for the divertor monoblock sample.

Name	Number of Voxels	Segmented Volume (x 10 ⁻⁹ m ³)	Surface area (x 10 ⁻⁶ m ²)	Number of Elements	Number of Nodes	Meshed Volume (x 10 ⁻⁹ m ³)
Monoblock (Original resolution, 21.8 x 10 ⁻⁶ m voxel width)						
Cu	42 M	434	723			
CFC	163 M	1690	3380			
Porosity	2.0 M	20.4	1560			
Gemco	1.2 M	12	592			
Total	208 M	2156.4	6255			
Monoblock (50% resolution, 43.6 x 10 ⁻⁶ m voxel width)						
Cu	5.2 M	0.23%	-1.38%	27 M	5.5 M	-0.95%
CFC	20 M	0.00%	-10.95%	106 M	22 M	-0.83%
Porosity	0.24 M	-2.45%	-23.08%	2.5 M	0.86 M	-37.31%
Gemco	0.14 M	0.00%	-0.84%	1.7 M	0.45 M	-1.15%
Total	26 M	0.02%	-11.91%	137 M	28 M	-1.20%

4.4 FEA

4.4.1 Case Study 1: CFC-Cu disc

Fig. 17 shows a temperature cross-section of the CFC-Cu disc during a simulation of the LFA, where the thermal pulse has partially propagated through the sample. Material properties used are given in Table 8.

Table 8

Material properties used for FEA.

Material	Conductivity (W·m ⁻¹ ·K ⁻¹)	Density (x 10 ³ kg·m ⁻³)	Specific Heat (x 10 ³ J·kg ⁻¹ ·K ⁻¹)
Cu	405.97	8.6098	0.555
CFC	232.43	1.7238	1.020
Gemco	24.300	8.8000	0.390
Porosity	0.0380	0.7380 E-03	1.030

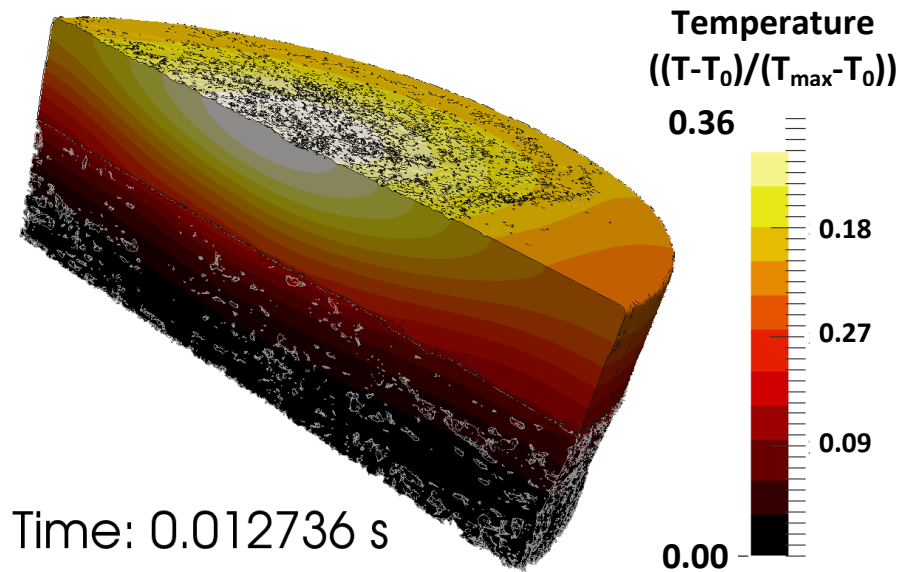


Fig. 17. Cross section of temperature within CFC-Cu sample at $t = 1.27 \times 10^{-2}$ s calculated by FEA.

Fig. 18 compares the results obtained for the CAD model, the low and high resolution IBFEM models and the experimental LFA. The results are normalised with respect to the initial and maximum temperatures to be comparable with experimental values (which are not available in absolute temperatures e.g. °C). This graph can be used to determine thermal diffusivity through the half rise time using the “Cowan + pulse correction” method [24].

The CAD model (Fig. 18) underestimates the sample’s thermal diffusivity by approximately 110 %. The low resolution IBFEM model which includes the largest pores and some surface detail underestimates the thermal diffusivity by approximately 30 %. The high resolution IBFEM provides the most accurate result, overestimating the thermal diffusivity by approximately 20 %. As predicted, the result shows a correlation between increasing model complexity and closeness to the experimental results.

In the high resolution analysis, the high diffusivity values (compared with the experimental results) may be due to the omission of some underlying thermodynamics. It is expected that model accuracy could be further improved by increasing the complexity of the simulation, achievable by the addition of features such as radiative boundary conditions, heat transfer coefficients, material properties that are temperature dependent or take into consideration anisotropic behaviour.

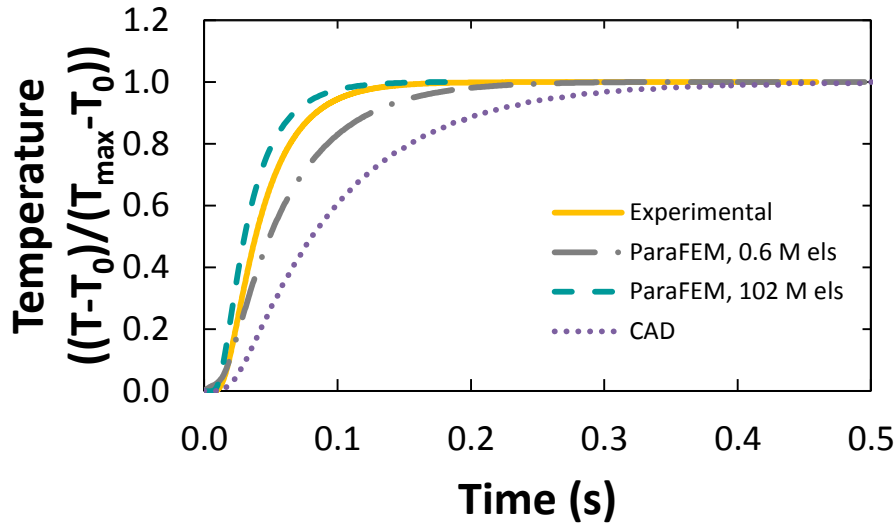


Fig. 18. Rear surface temperature of CFC-Cu disc during LFA experiment and simulation.

4.4.2 Case Study 2: Divertor monoblock

Fig. 19 shows a plot of the temperature at various time intervals for the divertor monoblock. Monoblocks usually exhibit hot spots at the corners of the loaded face [25], however in Fig. 19 there is a more even distribution of temperature. This is due to the debonding region causing a thermal barrier between the heat source and sink which is comparable to alternative monoblock concepts which include a thermal barrier by design [26] Fig. 20 shows temperature versus time in the CFC at a node located midway between the CFC-Cu interface and the sample edge where the thermal load is applied. Finite element analysis of the divertor monoblock was carried out in two orientations, firstly with the debonding region situated in line with the source (thermal loading) and the sink (Cu pipe) and secondly with the debonding region rotated by 180 ° with respect to this direction. When the debonding region was in line with the source and sink, temperatures in the debonding region exhibited a more extreme range of maxima and minima in comparison with the other orientation. This observation is supported by Fig. 21 and Fig. 22 which compare the temperature profile along a central line between the front and rear surfaces of the divertor monoblock at steady-state operation (i.e. $t = 5$ s) for both orientations.

In Fig. 22, the debonding creates a large thermal gradient at the boundary of the CFC and Cu by acting as a thermal barrier. This is more significant than the gradient caused by the relatively low conductivity of the Gemco layer. Zones of high thermal gradient will result in the generation of internal stresses. If aligned unfavourably in service, the debonding region would reduce the component's expected lifetime and increase the chance of failure.

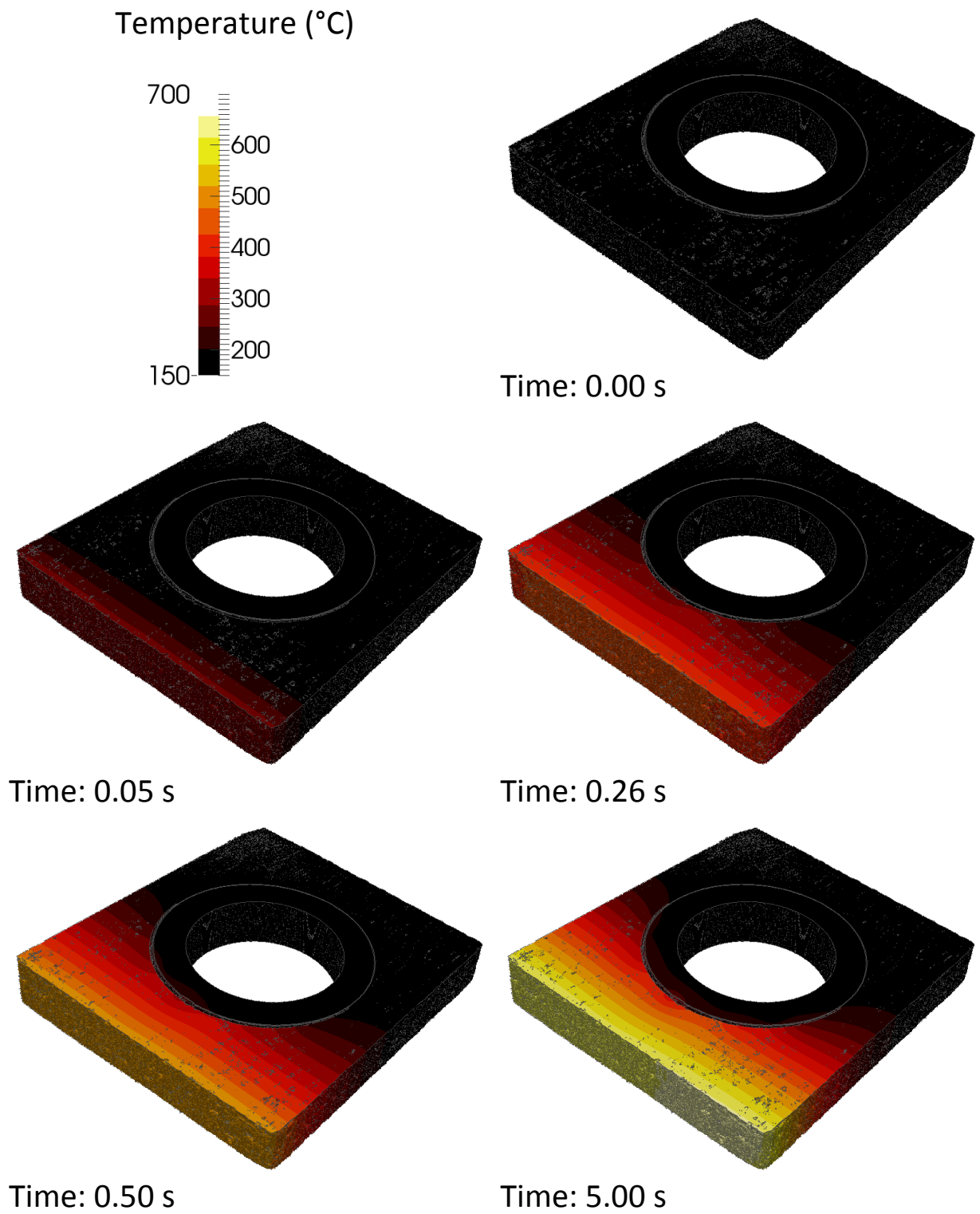


Fig. 19. Time series analysis of the divertor monoblock tile created from an X-ray tomography image.

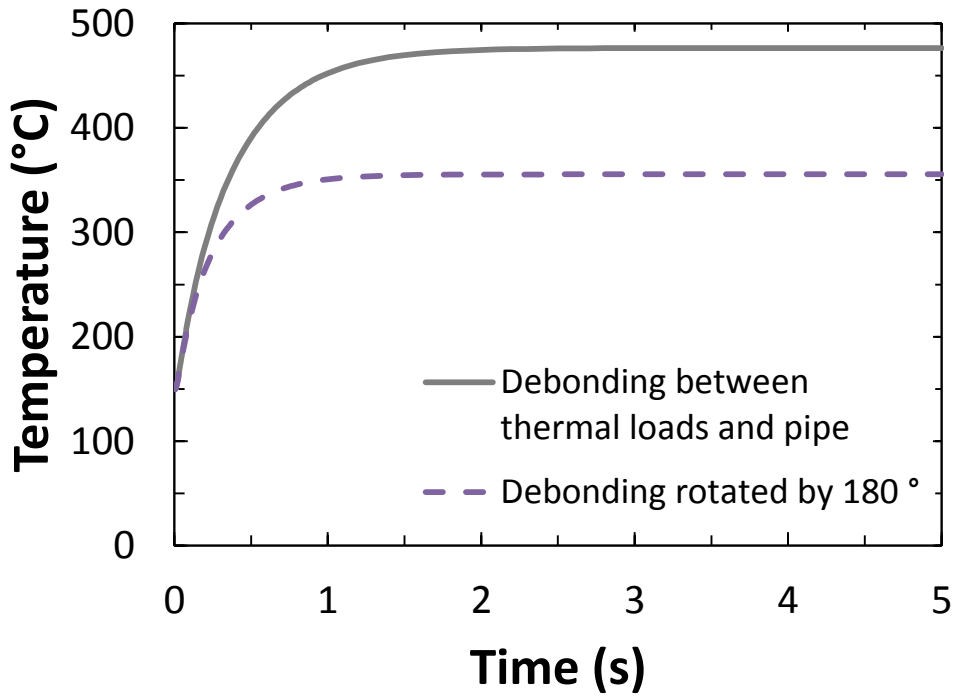


Fig. 20. Temperature of a node located centrally between the surface with applied thermal load and the CFC-Cu interface versus time for both orientations of the debonded region.

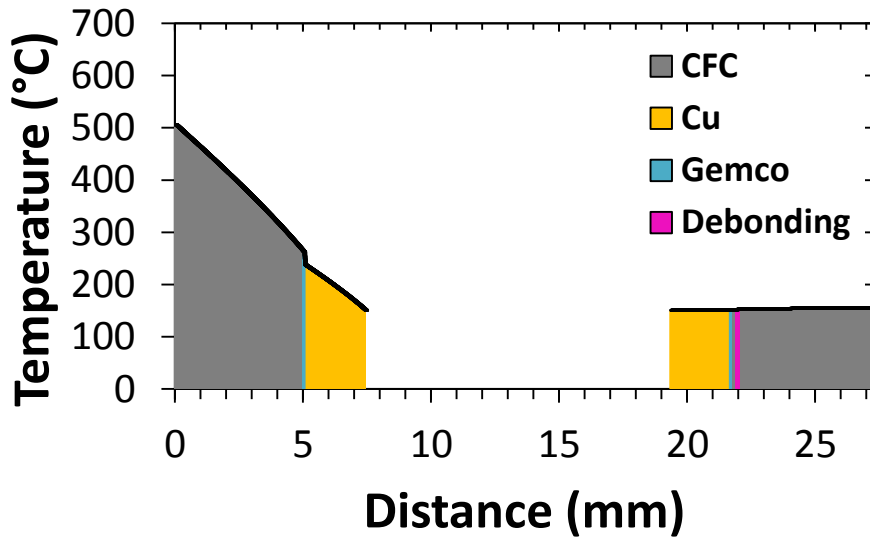


Fig. 21. Temperature profile between the front and rear surfaces of the divertor monoblock with debonding not aligned with the heat source and sink.

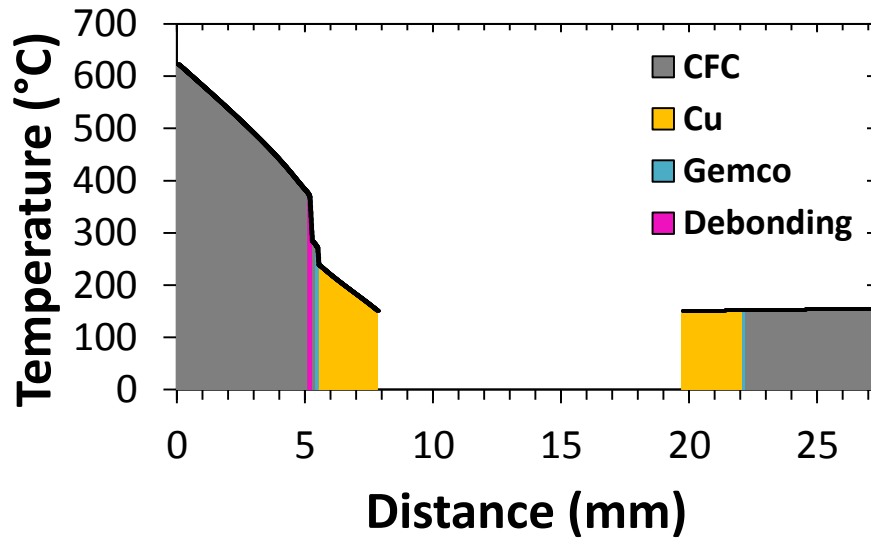


Fig. 22. Temperature profile between the front and rear surfaces of the divertor monoblock with debonding positioned between the Cu pipe and the thermal loads.

The porosity within the CFC had a less significant influence on the thermal behaviour. This is largely due to the favourable porosity alignment discussed earlier (shown in Fig. 15). At the micro-structural level, the finite element results in Fig. 23 show that the pores behave as thermal barriers causing “hot spots”. When the effect of these hot-spots is summed across the component, their contribution would be non-negligible. Regions surrounding the small veins of Cu had increased cooling opportunity and were therefore “cool spots”. These results show that reducing porosity and increasing Cu surface area is likely to improve efficiency, albeit the impact of this would be far outweighed by that of the presence of the debonding region.

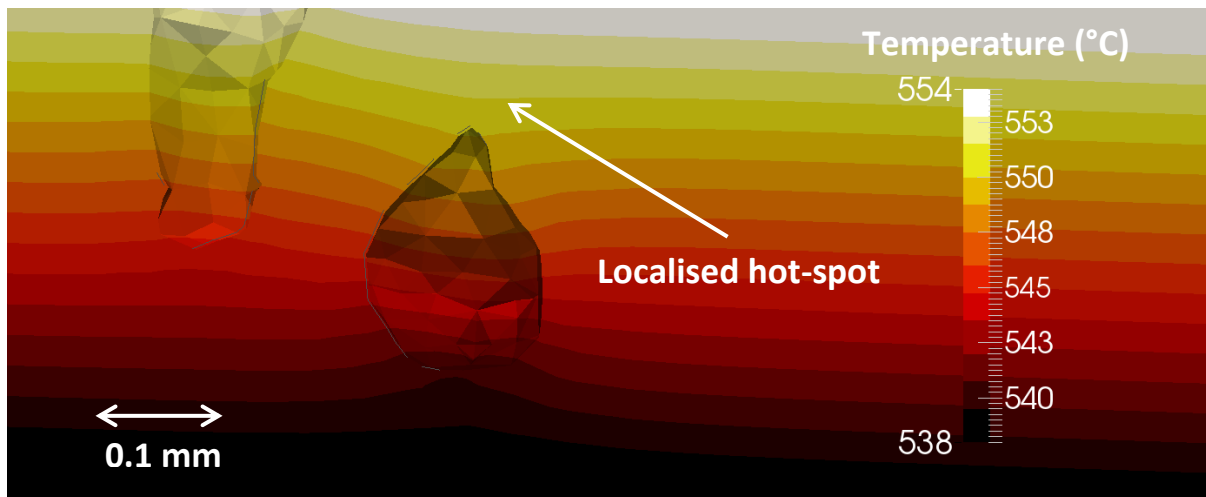


Fig. 23. Example of localised “hot spot” caused by porosity within the CFC.

5. Conclusions

In the first case study, laser flash analysis was carried out for a CFC-Cu disc where the interface had been joined by a novel brazing process using a Gemco foil pre-coated with chromium. It was shown that the thermal conductivity of the CFC-Cu disc decreased by 35% over a temperature range of

100 °C to 700 °C. This was in line with the average decrease of thermal conductivity for CFC and Cu. The thermal conductivity was little higher than that for CFC, which accounted for 57% of the sample's thickness, and not quite within the required parameters specified in the IMPH. This demonstrates the influence of the interface on thermal conductivity, and thus the importance of being able to predict the behaviour of the interface.

It was shown that high resolution image-based modelling of the LFA for the CFC-Cu disc provided a closer match with the experimental results than was achieved using traditional CAD based FEA. This verification and validation exercise demonstrated the reliability of the image-based modelling technique, and therefore confirmed its suitability for use in simulating conditions not easily reproduced in the laboratory, such as those expected in the ITER.

In the second case study, the CFC-Cu divertor monoblock, X-ray tomography highlighted difficulties in the manufacturing process by clearly showing the debonding of the CFC from the Cu pipe on one side of the interface. The image-based modelling, which captured this defect, showed that the debonding would result in lower thermal conductivity thus leading to a shorter life-expectancy and a higher chance of component failure due to increased internal stresses. Suggestions were made regarding improving component cooling efficiency such as: increasing the Cu surface area at the interface; reducing porosity; minimising the braze foil's thickness or selection of an alternative braze with higher thermal conductivity.

In the future, the image-based modelling techniques developed here could be used to simulate other scenarios expected in ITER, such as plasma instabilities or loss of coolant. Due to the nature of the technique it would also be easy to digitally alter the geometry to investigate the effect of varying porosity or interface properties.

The ParaFEM software together with the modifications required to carry out the research in this paper is freely available for download in source code form (see <http://www.parafem.org.uk>).

Acknowledgements

The authors would like to acknowledge support of the Engineering and Physical Sciences Research Council for the Fusion Doctoral Training Network (Grant EP/K504178/1) and Culham Centre for Fusion Energy (Grant EP/I501045). This work made use of HECToR (Project e254), the UK's national high-performance computing service, which is provided by UoE HPCx Ltd at the University of Edinburgh, Cray Inc and NAG Ltd, and funded by the Office of Science and Technology through EPSRC's High End Computing Programme. This work also made use of the facilities of N8 HPC provided by the N8 consortium under EPSRC Grant No.EP/K000225/1. The Centre is co-ordinated by the Universities of Leeds and Manchester. Access was also granted to the HPC resources of The Hartree Centre (project fusionFEM) made available within the Distributed European Computing Initiative (DECI-12) by the PRACE-2IP, receiving funding from the European Community's Seventh Framework Programme (FP7/2007-2013) under grant agreement RI-283493. Additionally, the authors would like to thank the Manchester X-ray Imaging Facility for use of tomography equipment, which was funded in part by the EPSRC (grants EP/F007906/1, EP/F001452/1 and EP/I02249X/1) and the staff at the University of Manchester for guidance in preparing this work.

References

- [1] A. Kukushkin, H. Pacher, V. Kotov, G. Pacher and D. Reiter, "Finalizing the ITER divertor design: The key role of SOLPS modeling," *Fusion Engineering and Design*, vol. 86, no. 12, pp. 2865-2873, 2011.
- [2] M. Merola and G. Vieider, "On the use of flat tile armour in high heat flux components," *Journal of Nuclear Materials*, vol. 258–263, no. Part 1, pp. 672-676, 1998.
- [3] R. Pitts, A. Kukushkin, A. Loarte, A. Martin, M. Merola and C. Kessel, "Status and physics basis of the ITER divertor," *Physica Scripta*, vol. T138, p. 014001, 2009.
- [4] "A blast of heat for ITER's plasma-facing components," [Online]. Available: <http://www.iter.org/newsline/251/1436>. [Accessed 31 July 2013].
- [5] Ll. M. Evans, L. Margetts, V. Casalegno, F. Leonard, T. Lowe, P. D. Lee, M. Schmidt and P. M. Mummery, "Thermal Characterisation of Ceramic/Metal Joining Techniques for Fusion Applications Using X-ray Tomography," *Fusion Engineering and Design*, vol. 89, no. 6, pp. 826-836, 2014.
- [6] V. Casalegno, T. Koppitz, G. Pintsuk, M. Salvo, S. Rizzo, S. Perero and M. Ferraris, "Proposal for a new brazing alloy for joining CFC composites to copper," *Composites Part B: Engineering*, vol. 56, pp. 882-888, 2014.
- [7] P. Appendino, V. Casalegno, M. Ferraris, M. Grattarola, M. Merola and M. Salvo, "Direct joining of CFC to copper," *Journal of Nuclear Materials*, Vols. 329-333, Part B, p. 1563–1566, 2004.
- [8] P. Appendino, M. Ferraris, V. Casalegno, M. Salvo and M. Merola, "Proposal for a new technique to join CFC composites to copper," *Journal of Nuclear Materials*, vol. 348, pp. 102-107, 2006.
- [9] J. Ali, C. Berre and P. M. Mummery, "Image based modelling of stress-strain behaviour in carbon/carbon composites," *Energy Materials: Materials Science and Engineering for Energy Systems*, vol. 1, no. 3, pp. 179-186, 2006.
- [10] P. Young, T. Beresford-West, S. Coward, B. Notarberardino, B. Walker and A. Abdul-Aziz, "An efficient approach to converting three-dimensional image data into highly accurate computational models," *Philosophical Transactions of The Royal Society A*, vol. 366, no. 1878, pp. 3155-3173, 2008.
- [11] S. Min, J. Blumm and A. Lindemann, "A new laser flash system for measurement of the thermophysical properties," *Thermochimica Acta*, vol. 455, no. 1-2, pp. 46-49, 2007.
- [12] "MXIF," [Online]. Available: <http://www.mxif.manchester.ac.uk/>. [Accessed 25 July 2013].
- [13] "3D images to RP, CAD, FE and CFD models with Simpleware software," [Online]. Available: <http://www.simpleware.com>. [Accessed 31 July 2013].

- [14] I. M. Smith, D. V. Griffiths and L. Margetts, *Programming the Finite Element Method 5th Ed.*, Chichester: Wiley, 2013.
- [15] "ParaFEM," [Online]. Available: <http://www.parafem.org.uk>. [Accessed 15 July 2013].
- [16] L.I. M. Evans, L. Margetts, J. Bushell, T. Lowe, A. Wallwork, W. E. Windes, P. Young and P. M. Mummery, "Parallel processing for time-dependent heat flow problems," in *NAFEMS World Congress*, Salzburg, Austria, 2013.
- [17] I. M. Smith and L. Margetts, "The Convergence Variability of Parallel Iterative Solvers," *Engineering Computations*, vol. 23, no. 2, pp. 154-165, 2006.
- [18] "xx12.f90 - parafem," [Online]. Available: https://code.google.com/p/parafem/source/browse/trunk/parafem/src/programs/dev/xx12_b/xx12_b.f90?r=1796. [Accessed 01 December 2014].
- [19] "Mechanical & Physical Properties," [Online]. Available: <http://www.wesgometals.com/resources/mechanical-physical-properties/>. [Accessed 31 July 2013].
- [20] W. M. Haynes, T. J. Bruno and D. R. Lide, "Thermophysical Properties of Air," in *94th Edition of the Handbook of Chemistry and Physics*, Boca Raton, FL, CRC Press/Taylor and Francis Group, 2013, pp. 6-18.
- [21] "ParaView - Open Source Scientific Visualization," [Online]. Available: <http://www.paraview.org/>. [Accessed 15 July 2013].
- [22] "ITER Materials Properties Handbook (MPH)," *ITER Doc. ITER_D_29DDCW (internal project document distributed to the ITER Participants)*.
- [23] J. Linke, M. Akiba, H. Bolt, G. Breitbach, R. Duwe, A. Makhankov, I. Ovchinnikov, M. Rödiger and E. Wallura, "Performance of Beryllium, Carbon and Tungsten under intensive thermal fluxes," *Journal of Nuclear Materials*, Vols. 241-243, pp. 1210-1216, 1997.
- [24] R. D. Cowan, "Pulse Method of Measuring Thermal Diffusivity at High Temperatures," *J. Appl. Phys.*, vol. 34, no. 4, pp. 926-927, 1963.
- [25] A. Herrmann, H. Greuner, M. Balden and H. Bolt, "Design and evaluation of an optimized W/Cu interlayer for W monoblock components," *Fusion Engineering and Design*, vol. 86, no. 1, pp. 27-32, 2011.
- [26] T. Barrett, D. Hancock, M. Kalsey, W. Timmis and M. Porton, "Design Study of a Water-Cooled Divertor: Alternative Concepts, Report for TA WP12-DAS-02-T02 [EFDA_D_2MA647]".